frontiers | Frontiers in Energy Research

TYPE Original Research
PUBLISHED 28 August 2023
DOI 10.3389/fenrg.2023.1257567

OPEN ACCESS

EDITED BY
Haopeng Song,
Nanjing University of Aeronautics and Astronautics, China

REVIEWED BY
Quanquan Yang,
Huaiyin Institute of Technology, China
Yan Shi,
Nanjing University of Aeronautics and Astronautics, China

*CORRESPONDENCE
Cheng Huang,
huangcheng@czu.cn
Jinbo Zhao,
zhaojb@czu.cn

RECEIVED 12 July 2023
ACCEPTED 14 August 2023
PUBLISHED 28 August 2023

CITATION
Huang C, Wang X and Zhao J (2023), Large electrocaloric effects induced by multidomain-to-monodomain transition in ferroelectrics with electrical inclusions. *Front. Energy Res.* 11:1257567. doi: 10.3389/fenrg.2023.1257567

Large electrocaloric effects induced by multidomain-to-monodomain transition in ferroelectrics with electrical inclusions

Cheng Huang[1]*, Xiaojun Wang[1] and Jinbo Zhao[2]*

[1]School of Aeronautical and Mechanical Engineering, Changzhou Institute of Technology, Changzhou, China, [2]School of Automotive Engineering, Changzhou Institute of Technology, Changzhou, China

The electrocaloric effect (ECE) depends on the sudden change of the polarization field during ferroelectric phase transition near the Curie temperature. Similarly, giant ECE can be found enormously during the domain structure transition from multidomain to monodomain process in ferroelectrics. To reveal the mechanism with the effects of the electric inclusions, the ECE of $PbTiO_3$ (PTO) ferroelectric solids under electric loads is investigated by phase-field simulation. The giant ECEs of ferroelectric materials containing three kinds of electric inclusions, namely, air, silicone oil, and water, are discussed in detail under applied electric fields. The results suggest that an unusual ultrahigh negative ECE (–9.30 K) and a large EC strength ($\Delta T/\Delta E$ = 0.237 KmMV^{-1}) are achieved near room temperature (about 50°C) in ferroelectrics containing water inclusion. The results indicate that electric inclusions generate high electrostatic energy under electric loads to break through the energy barrier and play an importation role in the ECE. In summary, the works may provide a better way to obtain the giant ECE and large EC strength close to room temperature by effectively regulating the dielectric constant of the electric inclusion and the increment of the applied electric field.

KEYWORDS

ferroelectrics, electrocaloric effect, phase-field simulation, multidomain-to-monodomain transition, electrical inclusion

1 Introduction

Solid-state refrigeration of ferroelectric materials has shown its low cooling energy density and high efficiency for miniaturization of electronic components. However, the low electrocaloric effect (ECE) and the limitation of the choice of ferroelectric materials hinder the application of the large ECE. With the giant ECE (12K) in the $Pb(Zr,Ti)O_3$ and polyvinylidene fluoride (PVDF) thin films (TFs) being obtained (Mischenko et al., 2006; Neese et al., 2008), the ferroelectric refrigeration has received more attention. After that, tremendous ECEs have been widely available in typical ferroelectrics such as PbTiO3 (PTO) (Qiu and Jiang, 2008), BaTiO3 (BTO) (Huang et al., 2018a), and lead-free $K_{1-x}Na_xNbO_3$ (KNN) (Zhao et al., 2020) by doping elements. A large number of experiments have found that the phase transition temperature of ferroelectric materials will sharply reduce to room temperature by element doping, which will also increase the operating temperature range of large ECEs .

With the development of experimental research on the ECE, multilayer composites (Qian et al., 2021; Liu et al., 2022a) and ceramic–polymer ferroelectric nanocomposites (Lich et al., 2020; Liu Y. et al., 2022b) can integrate the performance advantages of ferroelectric materials to strengthen the ECE and EC. Recently, molecular ferroelectric $ImClO_4$ and two-dimensional ferroelectric $CuInP_2S_6$ have shown excellent performance in electrocaloric refrigeration. Superior EC strength ($\Delta T/\Delta E = 0.84\,\mathrm{KmMV^{-1}}$) has been attained in molecular ferroelectric $ImClO_4$ with the unique polarization mechanism generated by the order–disorder behavior (Li et al., 2020). With the van der Waals layered structure in two-dimensional ferroelectric $CuInP_2S_6$, a large EC strength ($\Delta T/\Delta E = 0.295\,\mathrm{KmMV^{-1}}$) has been achieved (Si et al., 2019). These new electrocaloric materials are expected to become the development trend of high-performance ferroelectric solid-state refrigeration materials.

Different from ECEs actuated by ferroelectric–paraelectric phase transitions from the intrinsic factors of ion doping and material lamination, external stress–strain regulation can also significantly affect the change of the domain structure, eventually leading to large ECEs (Wang et al., 2014; Liu and Wang, 2015). The large ECEs generated by multidomain-to-monodomain transitions of PTO ferroelectrics under mismatch strains have been obtained by phase-field simulation (Hou et al., 2018). Most of the results show that in-plane polarization is produced by tensile mismatch strain, while out-of-plane polarization is affected by compressive strain. Different from the mismatch strain, the appropriate stress can also enhance the EC strength and increase the working temperature range of high EC strength (Wu et al., 2015).

Furthermore, the designed shape and structure of ferroelectrics can dramatically affect the ECEs. When the ferroelectric material contains cracks under the action of the electric field, a high electrostatic energy is generated in the cracks and the stress concentration near the tip of the cracks causes domain structure transition, thereby generating a giant ECE (Huang et al., 2021). So far, there are few research works on ferroelectric ECE with defects. In this paper, large ECEs induced by multidomain-to-monodomain transition in ferroelectrics with electrical inclusions are investigated based on the phase-field method. The main contents of the paper are arranged as follows: through the concise introduction, the phase-field model of ferroelectrics containing elliptical electric inclusion energy is given, and the unique electrical boundary conditions of the ferroelectric model containing electric inclusions are set in Section 2. The different giant ECEs formed by the ferroelectric model containing air, silicone oil, and water under the applied electric field are simulated, and the EC strength of the three models is analyzed in Section 3. Finally, the paper is summarized in Section 4.

2 Simulation methodology

Based on the Ginzburg–Landau phase transition theory, the total energy of the system is expressed as a function of time-dependent order parameters (Huang et al., 2018b). In particular, in order to simulate the influence of electrical inclusions on the evolution of the domain structure, the electrical inclusions are simulated as dielectrics filled with air, silicone oil, and water, which have negligible elastic energy. Then, the total electrical enthalpy h of the phase-field model includes Landau energy, gradient energy, stress–strain energy, electrostriction energy, electrostatic energy of ferroelectric solids, and electric inclusion, which can be expressed as follows:

$$\begin{aligned} h\left(P_i, P_{i,j}, \varepsilon_{ij}, E_i\right) = {} & a_i P_i^2 + a_{ij}^e P_i^2 P_j^2 + a_{ijk} P_i^2 P_j^2 P_k^2 + \frac{1}{2} G_{ijkl} P_{i,j} P_{k,l} \\ & + \frac{1}{2} c_{ijkl} \varepsilon_{ij} \varepsilon_{kl} - q_{ijkl} \varepsilon_{ij} P_k P_l - \frac{1}{2} \kappa_0 E_i E_i \\ & - E_i P_i - \frac{1}{2} \kappa_c E_i E_i, \end{aligned} \tag{1}$$

where a_i, a_{ij}^e, and a_{ijk} are the dielectric stiffness related to Landau energy and P_i is the polarization regarded as the first-order parameter. G_{ijkl} and $P_{i,j}$ denote the gradient coefficients and polarization gradient related to gradient energy, respectively. As the field variable of stress–strain energy, c_{ijkl} and ε_{ij} are expressed as the elastic stiffness constants and the strain, respectively. Similarly, q_{ijkl} and E_i are the field variables of electrostatic energy and denote the electrostrictive coefficients and electric field, respectively. It should be noted that κ_0 and κ_c are represented as the dielectric constant of matrix and electric inclusion, respectively.

Based on the basic principle of thermodynamics and Ginzburg–Landau equation, the mechanical equilibrium equation, electrical equilibrium equation, and phase-field dynamic equation can be expressed as follows (Huang et al., 2018a):

$$\frac{\partial}{\partial x_j}\left(\frac{\partial h}{\partial \varepsilon_{ij}}\right) = 0, \tag{2}$$

$$\frac{\partial}{\partial x_j}\left(-\frac{\partial h}{\partial E_i}\right) = 0, \tag{3}$$

$$\frac{\partial P}{\partial t} = -L\left[\frac{\partial h}{\partial P_i} - \left(\frac{\partial h}{\partial P_{i,j}}\right)_{,j}\right], \tag{4}$$

where x_j and t represent spatial and temporal, respectively. L represents the dynamic coefficient of the phase field. Here, the case with mechanical volume force and body charge is not considered. Thus, by integrating Eqs 2–4, the following weak solution forms are obtained:

$$\begin{aligned} \int_V \left\{\frac{\partial h}{\partial \varepsilon_{ij}}\delta\varepsilon_{ij} + \frac{\partial h}{\partial E_i}\delta E_i + \left[\frac{1}{L}\frac{\partial P_i}{\partial t} + \frac{\partial h}{\partial P_i}\right]\delta P_i + \frac{\partial h}{\partial P_{i,j}}\delta P_{i,j}\right\} \mathrm{d}V \\ = \int_s \left(T_i \delta u_i - \omega\delta\phi + \pi_i \delta P_i\right) \mathrm{d}S, \end{aligned} \tag{5}$$

where u_i and ϕ, as basic constant variables, represent the displacement and electric potential, respectively. T_i and ω, as dependent variables, denote the surface traction and surface charge, respectively. In order to simplify the expression, π_i is used instead of $\frac{\partial h}{\partial P_{i,j}} n_j$ to express the surface gradient energy flux. Based on the variational principle, the non-linear multifield coupling finite element method is adopted (Wang and Kamlah, 2009). The three-dimensional 8-node isoparametric element is used for spatial discretization, and the backward Euler iteration method is used for time integration to solve the non-linear equations. Finally, the physical field solutions are obtained by post-processing programming.

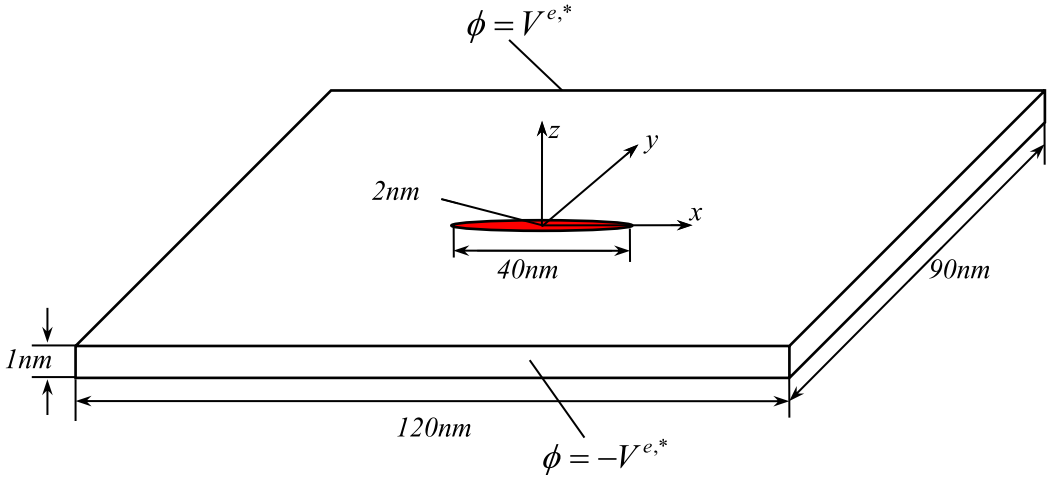

FIGURE 1
Schematic of a ferroelectric solid with inclusion.

Based on the phenomenological theory and thermodynamic principle, through the Maxwell relationship, when the external electric field is applied, the adiabatic temperature change (ΔT) is calculated by

$$\Delta T = -T\int_{E_a}^{E_b}\frac{1}{C_E(T,E)}\left(\frac{\partial P_i}{\partial T}\right)_E \mathrm{d}E_i \tag{6}$$

where $C_E(T,E)$ is the thermal capacity of ferroelectric materials. Based on the relevant experimental results (Liu and Wang, 2015), the thermal capacity of PTO can be set as a constant ($3.9 \times 10^6 \mathrm{Jm}^{-3}\mathrm{K}$) in this paper by ignoring the effect of the polarization field.

Figure 1 shows the overall schematic diagram of the ferroelectric plate with an electric inclusion under the applied electric field. As the phase-field model of this paper, the dimensionless sizes are set as follows: the length of the ferroelectric plate is 120, the width is 90, and the thickness is 1. The minimal thickness is set to degenerate the 3-D problem into the plane stress problem, which greatly simplifies the calculation process. The electric inclusion at the center is a flat ellipse, the long half axis of the electric inclusion is 20, and the short half axis is 1. It should be pointed out that in order to only reflect the influence of electrical inclusions on the domain structure, zero stress or strain loading is applied. The upper and lower electric potential values are set as $V^{e,*}$ and $-V^{e,*}$, respectively, where superscripts e and $*$ denote applied loading and dimensionless variable, respectively. Thus, the electric loads can be gained as $E^{e,*} = V^{e,*}/45$. The electrical boundary conditions of other surfaces can be set as the electrical open circuit (i.e., $D_i n_i = 0$). Since the model does not consider the application of mechanical loads, the traction-free condition is applied on each surface (i.e., $\sigma_{ij} n_j = 0$). The boundary condition for the polarization field is set to polarization-free on each surface $\left(\text{i.e., } \frac{\partial h}{\partial P_{i,j}} n_j = 0\right)$.

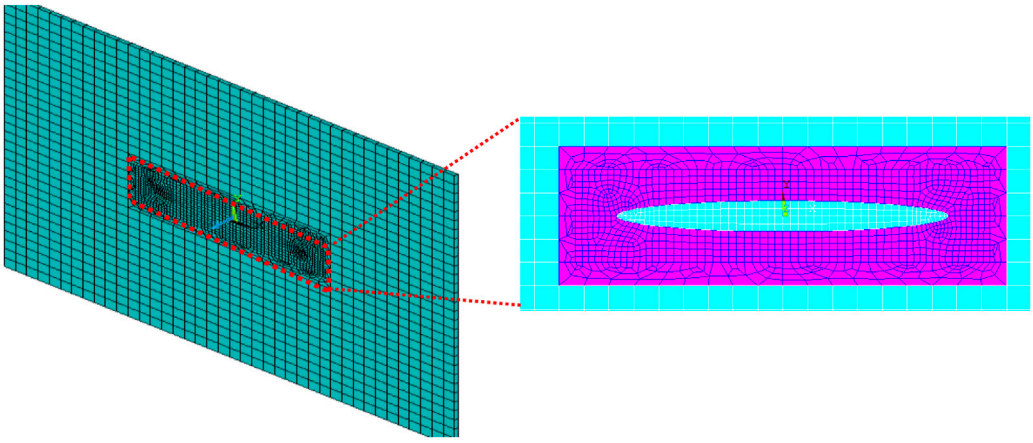

FIGURE 2
Mesh partitions of a simulated ferroelectric solid with an inclusion.

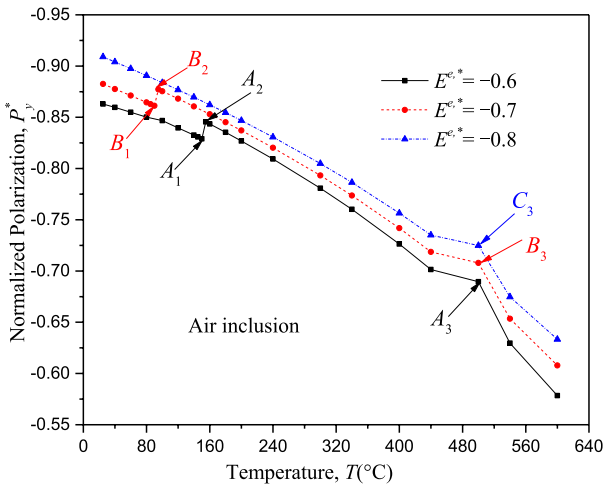

FIGURE 3
Polarization *vs.* temperature (*P*-*T*) curves of PTO with an air inclusion under different electric loads.

Figure 2 shows the mesh division of the model and the mesh densification at the crack tip, which results in the refined mesh size being much smaller than the domain wall size to ensure the correctness of the phase-field model. The material parameters of PTO in this paper are consistent with those in the previous work (Huang et al., 2018b). The dielectric constant of the medium in inclusion as air, oil, or water can be set as $\kappa_{c,air} = 8.854 \times 10^{-12}\mathrm{CV^{-1}m^{-1}}$, $\kappa_{c,oil} = 2.12 \times 10^{-11}\mathrm{CV^{-1}m^{-1}}$, and $\kappa_{c,water} = 7.099 \times 10^{-10}\mathrm{CV^{-1}m^{-1}}$, respectively. In order to be consistent with the material parameters of dimensionless stiffening, we set the following dimensionless field variables:

$$E^{e,*} = E^e/E^0\,(E^0 = 1306\,\mathrm{kV\,cm^{-1}}), P_y^* = P_y/P_0\,(P_0 = 0.757\mathrm{C\,m^{-2}}). \tag{7}$$

The initial polarization field direction is randomly distributed and the initial value is two orders of magnitude lower than that of the simulated polarization field, which is convenient to simulate the growth and enlargement of the ferroelectric domain structure, and finally form a steady-state evolution process. The dimensionless time step of the computational simulation is taken as $\Delta t = 0.04$.

3 Results and discussion

First, the ECE of the electric inclusion model containing air is simulated in this paper. Figure 3 shows the curve of the average

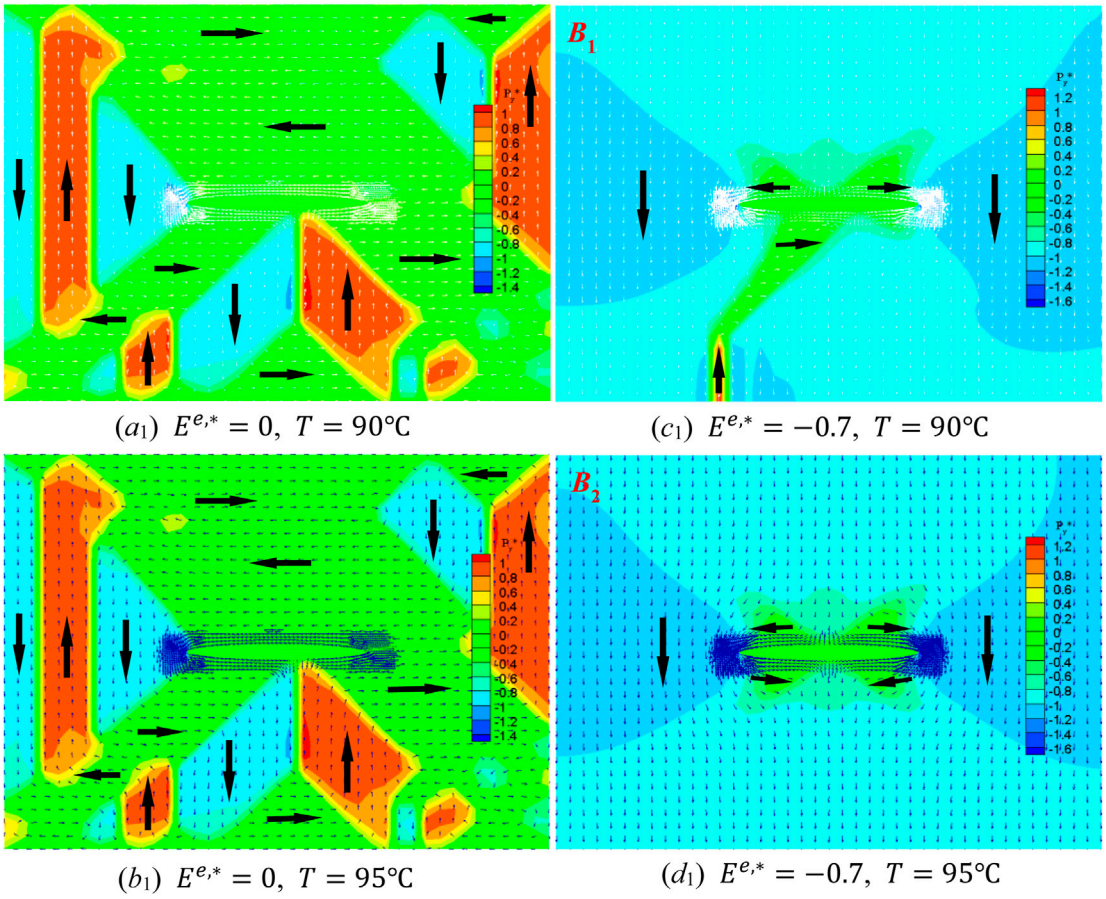

FIGURE 4
Domain structures of PTO under different electric loads near the transition temperature, which correspond to the points B_1-B_2.

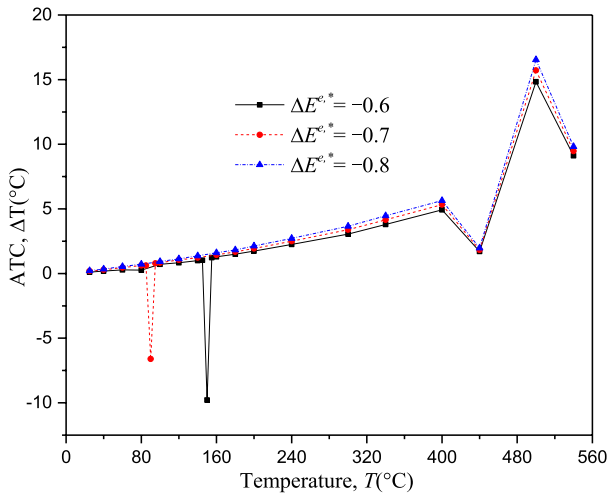

FIGURE 5
T-Δ*T* curves of the PTO with an air inclusion under different electric loads.

polarization field along the *y* direction with the temperature under the electric loads. The results show that the polarization field increases suddenly at $\boldsymbol{A_1}$-$\boldsymbol{A_2}$ and $\boldsymbol{B_1}$-$\boldsymbol{B_2}$, resulting in negative giant ECEs, which is consistent with the previous simulation results (Hou et al., 2018). The results also show that when the temperature exceeds 500°C, ferroelectric phase-to-paraelectric phase transition occurs in ferroelectric materials containing air inclusions, and the polarization field decreases sharply, resulting in positive giant ECEs.

In order to reveal the mechanism of large ECE through microstructure evolution, the detailed domain structures of PTO with an air inclusion are given in Figure 4 ($\boldsymbol{a}_1$)—($\boldsymbol{d}_1$), respectively. Under zero electric loads, the domain structure is in a head-to-tail state at different temperatures, which can greatly reduce the depolarization energy, as shown in Figure 4 ($\boldsymbol{a}_1$) and ($\boldsymbol{c}_1$). Figures 4 ($\boldsymbol{b}_1$) and ($\boldsymbol{d}_1$) exhibit the domain transition from the multidomain to monodomain state along the direction of the electric field ($E^{e,*} = 0.7$) during the ambient temperature rising from 90°C to 95°C, and only a winged 90° domain change is formed near the air inclusion. The giant strain energy and electrostatic energy could break through the energy barrier, and the sharp increase in the polarization field eventually leads to a negative giant ECE.

Figure 5 indicates that when the applied electric field changes, the average adiabatic temperature change has the largest negative ECE near the ambient temperature field ($E^{e,*} = 0.5$) of 150°C, and the temperature domain change produces a negative giant ECE ($\Delta T = -9.79$°C). When the temperature is close to the phase transition temperature of 500°C, a positive giant ECE is generated, and the temperature phase transition produces a positive giant ECE ($\Delta T = 14.83$°C). By increasing of the applied electric loads, a high electrostatic energy is generated in the air inclusion, and as a result, the domain transition temperature moves sharply to room temperature. The large negative ECE is generated ($\Delta T = -6.60$°C) near the temperature field of 90°C. It can be found that although the negative ECE obtained by increasing the electric field is slightly reduced, the temperature is greatly reduced, which is more conducive to engineering practice.

As we know, the air inclusion is apt to dielectric breakdown and produces a discharge phenomenon under high applied electric loads. Therefore, the inclusion is filled with silicone oil or water, which can effectively protect the ferroelectric material and improve the tolerance of the applied electric field strength. Figure 6 shows the temperature dependence of the polarization component $\boldsymbol{P}_2$ of PTO with oil and water inclusions under different electric loads. The results show that when the electric field is applied, the polarization field of the model containing silicone oil inclusion increases abruptly at $\boldsymbol{C_1}$-$\boldsymbol{C_2}$ and the water-inclusion model changes abruptly at $\boldsymbol{D_1}$-$\boldsymbol{D_2}$, all of which produce negative giant ECEs. Interestingly, the temperature for the giant ECE of the water-inclusion model is

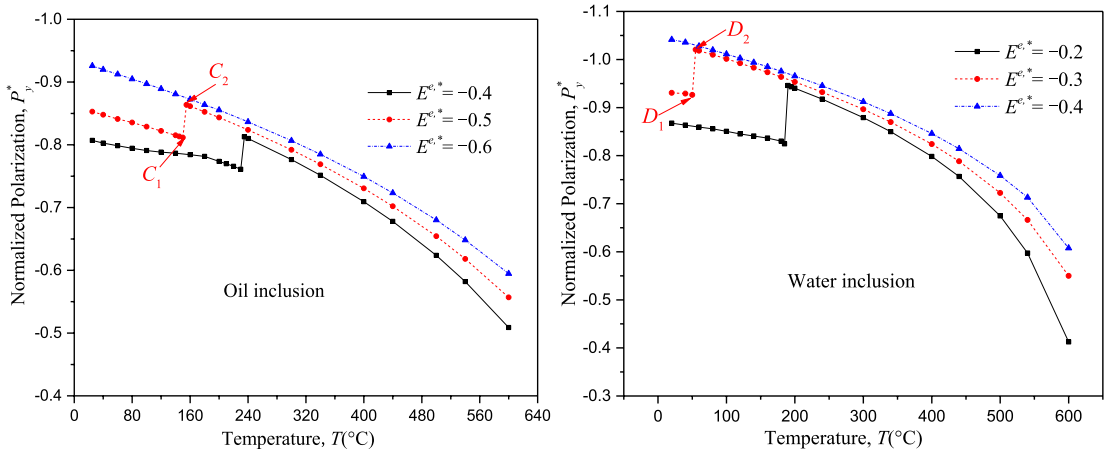

FIGURE 6
Comparison of the *P*-*T* curves of PTO with oil and water inclusions under different electric loads.

50°C, which effectively controls the temperature around the room temperature, which is convenient for experimental and engineering applications.

The detailed domain structures of PTO with oil and water inclusions at C_1-C_2 and D_1-D_2 to explain the mechanism of the giant ECE are shown in Figures 7, 8, respectively. The evolution of the microstructure reveals that the multidomain-to-monodomain transition is the result of energy minimization of the whole system under the coupling multifield, including the electric inclusion with high electrostatic energy, which explains the macroscopic behavior of the P-T curve in Figure 6 from the microscopic mechanism.

The adiabatic temperature change under different electric loads is shown in Figure 9 for the oil-inclusion and water-inclusion models. As shown in Figure 9, the peak value of negative ATC of the water-inclusion model at 50°C with ΔT = −9.30°C under relatively lower applied electric field (ΔE = 39.18MVm^{-1}). Table 1 summarizes the comparison of the giant ECE characterization parameters of the three electrical inclusion models with the literature results in detail. The results indicate that giant ECEs can be realized in the water-inclusion model near room temperature by effectively selecting the appropriate applied electric field increment. The current work may provide a fundamental understanding of domain transition and ECEs impacted by the electric inclusion and applied electric field.

4 Concluding remarks

In summary, the ECE of ferroelectric solids with different electric inclusions under electric loads is studied using a phase-field method. Numerical simulations show that the electric inclusion models containing air and silicone oil produce high electrostatic energy under applied electric field, and negative large ECEs are produced, but the domain transition temperature is much higher than room temperature. Because the dielectric constant of water and PTO are on the same order of magnitude, there is no electric field concentration inside the water inclusion, which only affects the distribution of the

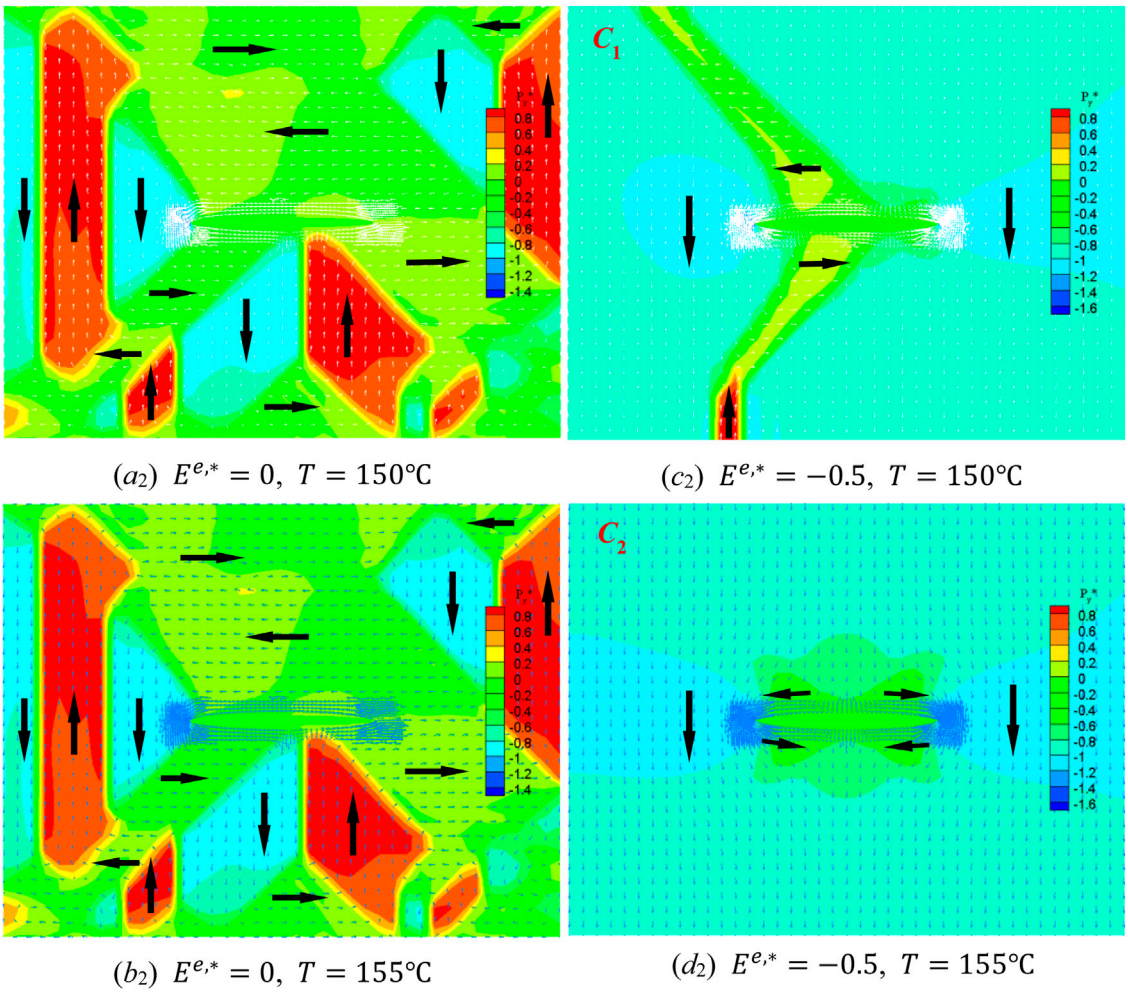

FIGURE 7
Domain structures of PTO under different electric loads near the transition temperature, which correspond to the points C_1-C_2

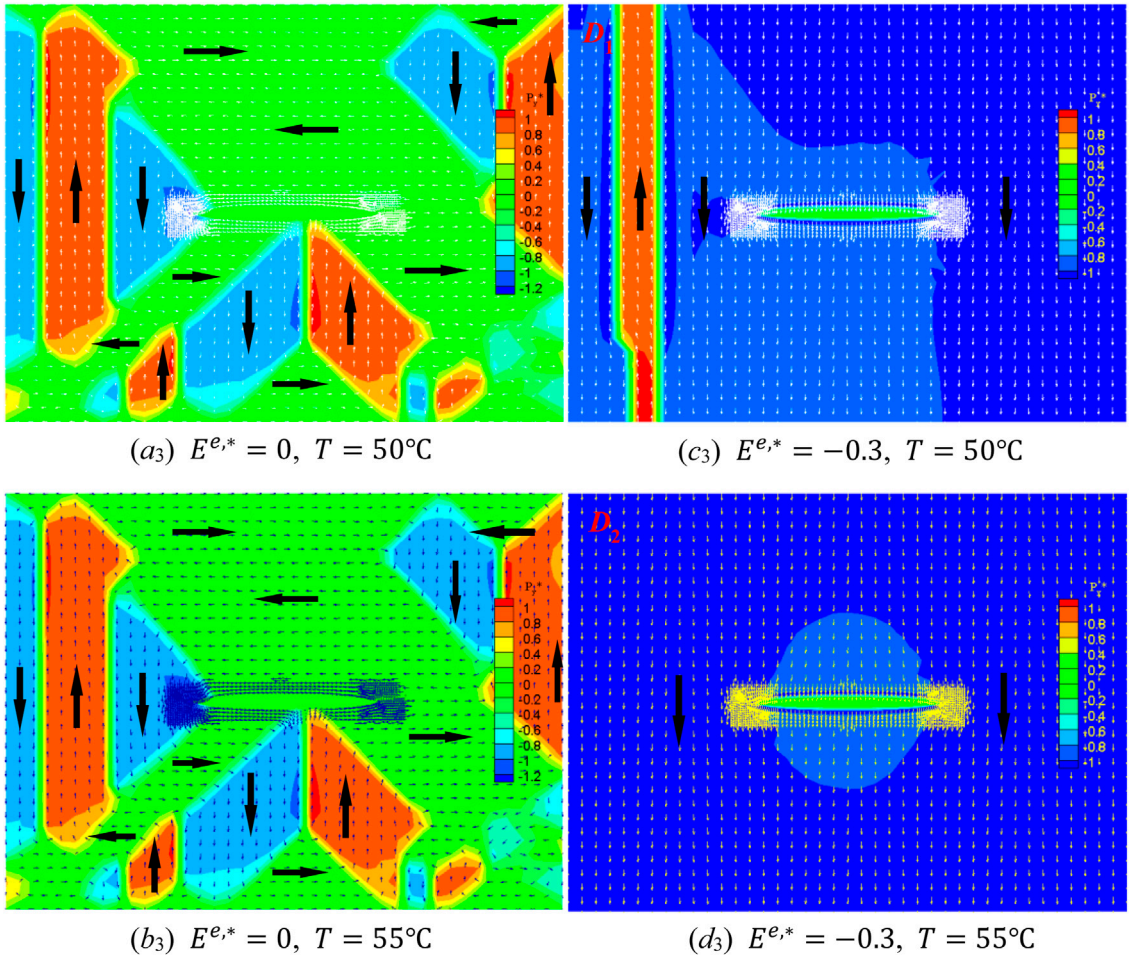

FIGURE 8
Domain structures of PTO under different electric loads near the transition temperature, which correspond to the points D_1-D_2

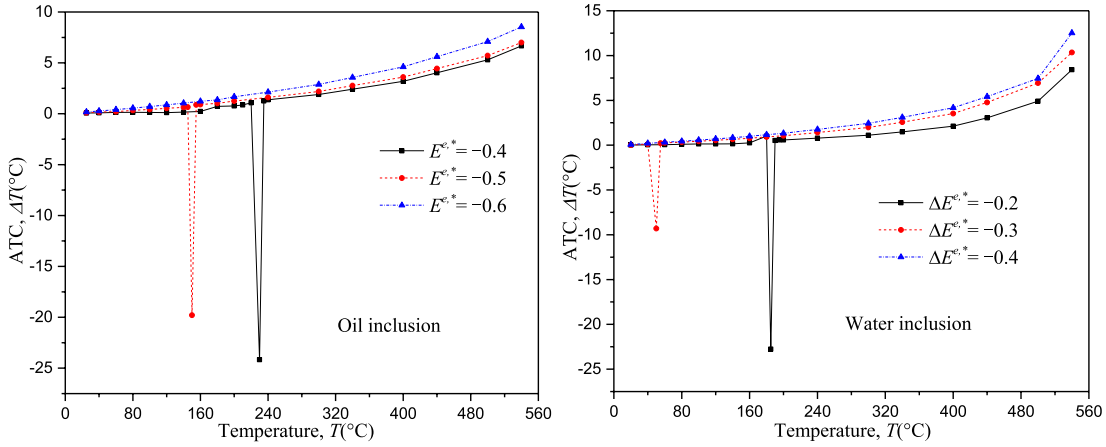

FIGURE 9
Comparison of T-ΔT curves of the PTO with oil and water inclusions under different electric loads.

TABLE 1 Comparison of ECEs of ferroelectrics with different electric inclusions.

Inclusions	T (°C)	ΔT (°C)	ΔE (MVm^{-1})	$\Delta T/\Delta E$ ($KmMV^{-1}$)
Air-1	150	−9.79	−78.36	0.125
Air-2	90	−6.60	−91.42	0.072
Air-3	500	16.54	−104.5	−0.158
Oil-1	230	−24.17	−52.24	0.459
Oil-2	150	−19.80	−65.3	0.303
Oil-3	540	8.53	−78.36	−0.102
Water-1	185	−22.76	−26.12	0.87
Water-2	50	−9.30	−39.18	0.237
Water-3	540	12.53	−52.24	−0.24
PTO (Hou et al., 2018)	290	−38.0	71.15	0.4
Cracked PTO (Huang et al., 2018a)	85	−7.55	39.2	0.193

polarization field of the model as a crack; thus, a ferroelectric solid with a water inclusion under relatively lower applied electric field ($\Delta E = 39.18 MVm^{-1}$), an unusual ultrahigh negative ECE (about −9.30 K), and a large EC strength ($\Delta T/\Delta E = 0.237\ KmMV^{-1}$) are obtained near room temperature (about 50°C). The present study provides a feasible way to regulate ECEs near room temperature under low electric loads by controlling the dielectric constant of electric inclusions in ferroelectrics.

Data availability statement

The original contributions presented in the study are included in the article/Supplementary Material. Further inquiries can be directed to the corresponding authors.

Author contributions

CH: formal analysis, methodology, writing–original draft, and writing–review and editing. XW: conceptualization and writing–review and editing. JZ: funding acquisition and writing–review and editing.

Funding

The authors declare financial support was received for the research, authorship, and/or publication of this article. The projects were supported by the National Natural Science Foundation of China (Grant No. 62273061), the Natural Science Foundation of the Jiangsu Higher Education Institutions of China (22KJA580001), and Qing Lan Project of Jiangsu Province of China (Grant No. 31120222003).

Conflict of interest

The authors declare that the research was conducted in the absence of any commercial or financial relationships that could be construed as a potential conflict of interest.

Publisher's note

All claims expressed in this article are solely those of the authors and do not necessarily represent those of their affiliated organizations, or those of the publisher, the editors, and the reviewers. Any product that may be evaluated in this article, or claim that may be made by its manufacturer, is not guaranteed or endorsed by the publisher.

References

Hou, X., Wu, H., Li, H., Chen, H., and Wang, J. (2018). Giant negative electrocaloric effect induced by domain transition in the strained ferroelectric thin film. *J. Phys. Condens Matter.* 30 (46), 465401. doi:10.1088/1361-648X/aae602

Huang, C., Yang, H. B., and Gao, C. F. (2018b). Giant electrocaloric effect in a cracked ferroelectrics. *J. Appl. Phys.* 123 (15), 154102. doi:10.1063/1.5004203

Huang, C., Yin, M. S., Qi, X., and Guo, H. (2021). Torsion of circular shaft with elliptical inclusions or cracks. *Trans. Nanjing Univ. Aeronautics Astronautics* 38 (1), 96–105. doi:10.16356/j.1005-1120.2021.01.009

Huang, Y. H., Wang, J. J., Yang, T. N., Wu, Y. J., Chen, X. M., and Chen, L. Q. (2018a). A thermodynamic potential, energy storage performances, and electrocaloric effects of $Ba_{1-x}Sr_xTiO_3$ single crystals. *Appl. Phys. Lett.* 112 (10), 102901. doi:10.1063/1.5020515

Li, W. R., Jafri, H. M., Zhang, C., Zhang, Y. J., Zhang, H. B., Huang, H. B., et al. (2020). The strong electrocaloric effect in molecular ferroelectric $ImClO_4$ with ultrahigh electrocaloric strength. *J. Mat. Chem. A* 8 (32), 16189–16194. doi:10.1039/d0ta05154c

Lich, L. V., Vu, N. L., Ha, M. T., Bui, T. Q., Le, V. T., Nguyen, T. G., et al. (2020). Enhancement of electrocaloric effect in compositionally graded ferroelectric nanowires. *J. Appl. Phys.* 127 (21), 214103. doi:10.1063/1.5145040

Liu, M., and Wang, J. (2015). Giant electrocaloric effect in ferroelectric nanotubes near room temperature. *Sci. Rep.* 5, 7728. doi:10.1038/srep07728

Liu, Y. Q., Liu, J. F., Pan, H., Cheng, X. X., Hong, Z. J., Xu, B., et al. (2022a). Phase-field simulations of tunable polar topologies in lead-free ferroelectric/paraelectric multilayers with ultrahigh energy-storage performance. *Adv. Mat.* 34, 2108772. doi:10.1002/adma.202108772

Liu, Y., Yang, T. N., Zhang, B., Williams, T., Lin, Y. T., Li, L., et al. (2022b). Structural insight in the interfacial effect in ferroelectric polymer nanocomposites. *Adv. Mat.* 34 (7), 2109926. doi:10.1002/adma.202109926

Mischenko, A. S., Zhang, Q., Scott, J. F., Whatmore, R. W., and Mathur, N. D. (2006). Giant electrocaloric effect in thin-film $PbZr_{0.95}Ti_{0.05}O_3$. *Science* 311 (5765), 1270–1271. doi:10.1126/science.1123811

Neese, B., Chu, B. J., Lu, S. G., Wang, Y., Furman, E., and Zhang, Q. M. (2008). Large electrocaloric effect in ferroelectric polymers near room temperature. *Science* 321 (5890), 821–823. doi:10.1126/science.1159655

Qian, X. S., Han, D. L., Zheng, L. R., Chen, J., Tyagi, M., Li, Q., et al. (2021). High-entropy polymer produces a giant electrocaloric effect at low fields. *Nature* 600, 664–669. doi:10.1038/s41586-021-04189-5

Qiu, J. H., and Jiang, Q. (2008). Effect of electric field on electrocaloric effect in $Pb(Zr_{1-x}Ti_x)O_3$ solid solution. *Phys. Lett. A* 372 (48), 7191–7195. doi:10.1016/j.physleta.2008.10.042

Si, M. W., Saha, A. K., Liao, P. Y., Gao, S. J., Neumayer, S. M., Jian, J., et al. (2019). Room-temperature electrocaloric effect in layered ferroelectric $CuInP_2S_6$ for solid-state refrigeration. *ACS Nano* 13 (8), 8760–8765. doi:10.1021/acsnano.9b01491

Wang, J., and Kamlah, M. (2009). Three-dimensional finite element modeling of polarization switching in a ferroelectric single domain with an impermeable notch. *Smart Mat. Struct.* 18, 104008. doi:10.1088/0964-1726/18/10/104008

Wang, J., Liu, M., Zhang, Y., Shimada, T., Shi, S. Q., and Kitamura, T. (2014). Large electrocaloric effect induced by the multi-domain to mono-domain transition in ferroelectrics. *J. Appl. Phys.* 115 (16), 164102. doi:10.1063/1.4873112

Wu, H. H., Zhu, J., and Zhang, T. Y. (2015). Pseudo-first-order phase transition for ultrahigh positive/negative electrocaloric effects in perovskite ferroelectrics. *Nano Energy* 16, 419–427. doi:10.1016/j.nanoen.2015.06.030

Zhao, X. Y., Wang, J. J., and Chen, L. Q. (2020). A thermodynamic study of phase transitions and electrocaloric properties of $K_{0.5}Na_{0.5}NbO_3$ single crystals. *Appl. Phys. Lett.* 116 (9), 092902. doi:10.1063/1.5144056